FRB–SRB–XRB: Geometric and Relativistic Beaming Constraints of Fast Radio Bursts from the Galactic Magnetar SGR J1935+2154

Connery J. Chen,[1,2]* Bing Zhang,[1,2]†

[1]*Nevada Center for Astrophysics, University of Nevada, Las Vegas, NV 89154, USA*
[2]*Department of Physics and Astronomy, University of Nevada, Las Vegas, NV 89154, USA*

ABSTRACT

The detection of a fast radio burst (FRB), FRB 200428, coincident with an X-ray burst (XRB) from the Galactic magnetar soft gamma repeater (SGR) SGR J1935+2154 suggests that magnetars can produce FRBs. Many XRBs have been detected from the source, but very few were found to be associated with bursty radio emission. Meanwhile, a number of weaker radio bursts have been detected from the source, which could in principle be slow radio bursts (SRBs): FRBs detected at viewing angles outside the FRB jet cone. In this paper, we use these X-ray and radio observations to constrain the geometric and relativistic beaming factors of FRBs under two hypotheses. First, we assume that all SRBs should be associated with XRBs like FRB 200428. We use the FRB–SRB closure relations to identify two SRBs and derive that FRB beaming must be geometrically narrow, $\theta_j \lesssim 10^{-2}$ rad, and follow $\theta_j \Gamma \sim 2$. Second, we assume a less stringent constraint for SRBs by not requiring that they are associated with XRBs. We identify a total of seven SRBs, five of which have Gaussian-like spectra, and derive that FRB beaming factors again follow $\theta_j \Gamma \sim 2$.

Key words: fast radio bursts – magnetars

1 INTRODUCTION

On 2020 April 28, a 1.5 MJy fast radio burst (FRB) originating from the Galactic magnetar SGR J1935+2154 was detected by the Suvery for Transient Astronomical Radio Emission (STARE2) radio array and Canadian Hydrogen Intensity Mapping Experiment (CHIME) at equal arrival times (Bochenek et al. 2020b; The CHIME/FRB Collaboration 2020). This event is referred to as FRB 200428. Remarkably, a hard X-ray burst (XRB) was independently detected by Insight–HXMT, INTEGRAL, AGILE, and Konus-Wind (Li et al. 2021; Mereghetti et al. 2020; Tavani et al. 2021; Ridnaia et al. 2021). It was the first associated FRB–XRB event ever detected; whether it was an intrinsically unique event from the majority of FRB-absent SGR bursts is still subject to debate (i.e., Yang et al. 2021). Extensive monitoring of the source in radio and X-ray bands has enabled investigations on whether the observed scarcity might be due to beaming (Lin et al. 2020a; Scholz et al. 2017).

The Five-hundred-meter Aperture Spherical Telescope (FAST) first observed SGR J1935+2154 on 2020 April 15 UTC 21:54:29 and began monitoring the source daily on 2020 April 26 UTC 21:06:55. FAST was not monitoring SGR J1935+2154 at the time of FRB 200428. On 2020 April 30 UTC 21:43:00.42, FAST detected one weak and highly polarized radio emission from the source (Zhang et al. 2020). During the observation windows conducted by FAST in April, the Fermi Gamma-ray Burst Monitor (Fermi/GBM) reported 34 XRBs from SGR J1935+2154 (Yang et al. 2021) and the Neutron star Interior Composition Explorer (NICER) reported 121, 104

of which are unique from the Fermi/GBM detections (Younes et al. 2020). FAST continued to monitor the source almost daily until May 19 but detected no additional radio signals (Zhu et al. 2022). During these extended observations, Insight–HXMT detected two XRBs from the source on May 6 and May 12 (Cai et al. 2022a). Numerous non-detections of radio emission by FAST during SGR bursting events indicate that FRB–XRB associations are exceptionally rare.

Targeted observations in the following months of 2020 by the Westerbork Radio Telescope 1 (RT1), the Northern Cross at the Medicina Radio Astronomical Station (Medicina Northern Cross; MNC), CHIME, FAST, and the Big Scanning Array of Lebedev Physical Institute (BSA/LPI) yielded several additional weak radio bursts (Kirsten et al. 2021; Burgay et al. 2020; Good & Chime/Frb Collaboration 2020; Zhu et al. 2020; Alexander & Fedorova 2020). None of the radio detections following FRB 200428 were found to be associated with an XRB.

In early October, 2022, SGR J1935+2154 entered another active bursting phase (Palm 2022). At least two additional weak radio bursts were detected from the source (Dong & Chime/Frb Collaboration 2022; Huang et al. 2022), both accompanied by simultaneous XRB detections (Wang et al. 2022b; Li et al. 2022b).

In Section 2 we reiterate the theory of SRBs introduced in Zhang (2021), extend the application to FRBs with a Gaussian spectrum and discuss FRB beaming constraints by SRB detectability. In Section 3 we review FRB beaming constraints by non-detections of radio emission by FAST concurrent with XRBs (e.g., Lin et al. 2020a) and extend the models to FRBs with a Gaussian spectrum. A collection of observational data is presented in Section 4. The theoretical models are applied to observational data under two hypotheses, discussed in Section 5. The conclusions are presented in Section 6.

* E-mail: chenc38@unlv.nevada.edu
† E-mail: bing.zhang@unlv.edu

2 ON-BEAM FRB VS. OFF-BEAM SRB

The original definition and description of SRBs is presented in Zhang (2021). SRB theory considers geometric and relativistic beaming factors for FRBs. Current FRB emission models postulate that relativistically moving plasma produces the FRB emission (Zhang 2020, and references therein). When such emission is beamed (non-isotropic), SRBs should be detectable.

Observations suggest that at least some FRBs, especially repeating sources, have intrinsically narrow spectra consistent with a Gaussian shape (e.g., Aggarwal et al. 2021; Pleunis & CHIME/FRB Collaboration 2020). In this work we extend the theories to apply to FRBs with narrow Gaussian spectra.

2.1 Doppler factor

Consider a relativistic conical jet with bulk Lorentz factor Γ (corresponding to dimensionless speed β) and half opening angle θ_j. Also consider an observer viewing at some angle θ from the jet axis. The Doppler Factor can be defined as

$$\mathcal{D}(\theta) = \begin{cases} \mathcal{D}_{\text{on}} = \frac{1}{\Gamma(1-\beta)}, & \theta < \theta_j \\ \mathcal{D}_{\text{off}} = \frac{1}{\Gamma(1-\beta\cos[\Delta\theta])}, & \theta > \theta_j \end{cases} \quad (1)$$

where $\Delta\theta = \theta - \theta_j$ (Zhang 2021). In a relativistic context, the Doppler factor connects observer-frame (unprimed) quantities with comoving-frame (primed) quantities (e.g., Zhang (2018))

$$\Delta t = \mathcal{D}^{-1}\Delta t' \quad (2)$$
$$\nu = \mathcal{D}\nu' \quad (3)$$
$$L_\nu(\nu) = \mathcal{D}^3 L'_{\nu'}(\nu') \quad (4)$$

where Δt is the emission duration, ν is the emission frequency, and L_ν is the isotropic-equivalent specific luminosity. The last expression assumes a point source for which all emitter material is moving towards one direction. This is justified for FRBs because the emission region is very small.

Consider two observers, one viewing the jet at an on-axis angle $\theta \leq \theta_j$ so that $\mathcal{D} = \mathcal{D}_{\text{on}}$, and the other viewing the jet at an off-axis angle $\theta \geq \theta_j$ so that $\mathcal{D} = \mathcal{D}_{\text{off}}$. As in Zhang (2021), we compare the observed properties by defining a ratio of Doppler factors

$$\mathcal{R}_\mathcal{D} \equiv \frac{\mathcal{D}_{\text{on}}}{\mathcal{D}_{\text{off}}} \geq 1. \quad (5)$$

Assuming that the comoving-frame parameters are identical for both on- and off-axis observers, $\mathcal{R}_\mathcal{D}$ directly relates the on-beam FRB properties with the off-beam SRB properties. The general geometry of the beaming interpretation is shown in Fig. 1.

In this work we only consider a narrow Gaussian-like spectrum for FRBs in the rest-frame. The specific luminosity spectrum (e.g., Zhang 2021) is

$$L'_{\nu'}(\nu') = L'_{\nu'}(\nu'_0) \exp\left[-\frac{1}{2}\left(\frac{\nu'-\nu'_0}{\delta\nu'}\right)^2\right] \quad (6)$$

where ν'_0 and $\delta\nu'$ are the central frequency and characteristic width of the spectrum, respectively. In the case of a narrow spectrum, $\delta\nu'/\nu' \ll 1$.

2.2 FRB–SRB closure relation

Consider again one on-axis FRB observer and one off-axis SRB observer. For an FRB (SRB) with specific fluence $\mathcal{F}_\nu^{\text{FRB}}$ ($\mathcal{F}_\nu^{\text{SRB}}$),
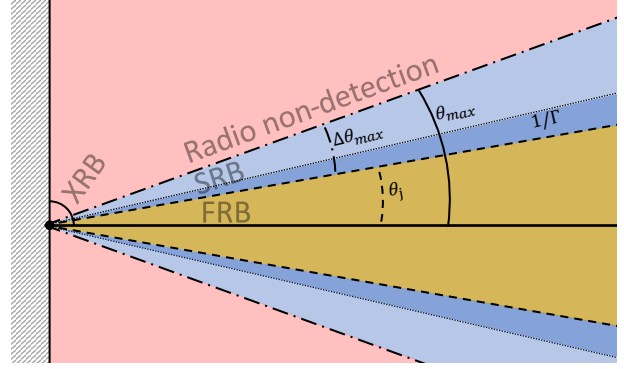
Figure 1. Geometry of the FRB–SRB–XRB beaming interpretation. A beamed FRB (*gold, dashed*) with half-opening angle θ_j is detectable as an off-axis SRB to a certain maximum angle beyond the jet cone $\Delta\theta_{\max}$ (*blues, dash-dotted*), corresponding to a maximum viewing angle from the jet axis, $\theta_{\max} = \Delta\theta_{\max} + \theta_j$ (*black, solid*). A viewing angle beyond $1/\Gamma$ (dark-blue, dotted) will witness a rapid decline in SRB fluence. Beyond $\theta_{\max}$, in the red region, an observer will not detect any radio signal, but instead will only detect the associated XRB emitted across 2π steradians. The radio emission region is, at maximum, 2π steradians, (in this geometric representation, $\theta_{\max} \leq \pi/2$). The hatched region behind the emission site is beyond the possible region of emission in this orientation. The magnetar source is assumed to be a point source, represented by the black dot.

intrinsic width w^{FRB} (w^{SRB}), and observing frequency at ν_1 (ν_2), one may assume $\nu_1 = \mathcal{D}_{\text{on}}\nu'_0 = \nu^{\text{FRB}}$ ($\nu_2 = \mathcal{D}_{\text{off}}\nu'_0 = \nu^{\text{SRB}}$). Using equation 6 together with the above, the ratio of specific luminosities can be written as

$$\frac{L_\nu^{\text{off}}(\nu_2)}{L_\nu^{\text{on}}(\nu_1)} = \frac{\mathcal{D}_{\text{off}}^3}{\mathcal{D}_{\text{on}}^3} \frac{\exp\left[-\frac{1}{2}\left(\frac{\nu_2-\nu^{\text{off}}}{\delta\nu^{\text{off}}}\right)^2\right]}{\exp\left[-\frac{1}{2}\left(\frac{\nu_1-\nu^{\text{on}}}{\delta\nu^{\text{on}}}\right)^2\right]}$$
$$= \mathcal{R}_\mathcal{D}^{-3} \exp\left\{-\frac{1}{2}\left[\left(\frac{\nu'_2-\nu'_0}{\delta\nu'}\right)^2 - \left(\frac{\nu'_1-\nu'_0}{\delta\nu'}\right)^2\right]\right\} \quad (7)$$

(Zhang 2021). For an on-axis FRB observer, one may assume that the observing frequency is at the central frequency of the spectrum, i.e., $\nu'_0 = \nu'_1$. Simplifying equation 7, one arrives at an expression for the luminosity ratio between the off-axis SRB and on-axis FRB observers.

$$\frac{L_\nu^{\text{off}}(\nu_2)}{L_\nu^{\text{on}}(\nu_1)} = \mathcal{R}_\mathcal{D}^{-3} \exp\left\{-\frac{1}{2}\left[\left(\frac{\nu'_2-\nu'_1}{\delta\nu'}\right)^2\right]\right\}$$
$$= \mathcal{R}_\mathcal{D}^{-3} \exp\left[-\frac{1}{2}\left(\frac{\frac{\nu_2}{\mathcal{D}_{\text{off}}} - \frac{\nu_1}{\mathcal{D}_{\text{on}}}}{\frac{\delta\nu_{\text{on}}}{\mathcal{D}_{\text{on}}}}\right)^2\right]$$
$$= \mathcal{R}_\mathcal{D}^{-3} \exp\left[-\frac{1}{2}\left(\frac{\nu_1}{\delta\nu_{\text{on}}}\right)^2\left(\mathcal{R}_\mathcal{D}\frac{\nu_2}{\nu_1} - 1\right)^2\right]. \quad (8)$$

Noticing that $\mathcal{R}_\mathcal{D} = w^{\text{off}}/w^{\text{on}}$, Zhang (2021) obtains a closure relation for this ratio

$$\left(\frac{F_\nu^{\text{SRB}}}{F_\nu^{\text{FRB}}}\right)\left(\frac{w_\nu^{\text{SRB}}}{w_\nu^{\text{FRB}}}\right)^2 \exp\left[\frac{1}{2}\left(\frac{\nu^{\text{SRB}}}{\delta\nu^{\text{FRB}}}\right)^2\left(\frac{w^{\text{SRB}}}{w^{\text{FRB}}} - 1\right)^2\right] = 1. \quad (9)$$

For data sets that span many orders of magnitude, as is usually the case when dealing with FRBs and SRBs, it is more feasible to

consider a logarithmic form of the closure relation, i.e.,

$$\ln\left(\frac{F_\nu^{\text{SRB}}}{F_\nu^{\text{FRB}}}\right) + 2\ln\left(\frac{w_\nu^{\text{SRB}}}{w_\nu^{\text{FRB}}}\right) + \left[\frac{1}{2}\left(\frac{\nu^{\text{SRB}}}{\delta\nu^{\text{FRB}}}\right)^2\left(\frac{w^{\text{SRB}}}{w^{\text{FRB}}} - 1\right)^2\right] = 0. \quad (10)$$

Equations 9 or 10 can be used to determine whether observed radio pulses are off-axis SRB viewings of on-axis FRBs. In case we must use equation 10 due to computational limits, we confirm unity by equating it to the parameter, $u = \log(1 + \epsilon) \approx 0$ where $\epsilon \ll 1$.

2.3 SRB Detectability

Beyond the FRB jet cone, θ_j, the specific fluence of an off-axis SRB diminishes rapidly and the pulse duration increases. The variation depends on the intrinsic beaming factors of the FRB. FRB emission models invoke a highly relativistic plasma, $\Gamma \gtrsim 10^2$ (Lyubarsky 2008; Murase et al. 2016; Lu & Kumar 2018; Zhang 2022b) to produce the FRB emission, and may be narrowly beamed along open magnetic field lines if the emission region is within the magnetosphere (Kumar et al. 2017; Yang & Zhang 2018; Metzger et al. 2019; Wadiasingh & Timokhin 2019; Wang et al. 2020; Kumar & Bošnjak 2020; Lu et al. 2020; Yang et al. 2020; Wadiasingh et al. 2020; Qu & Zhang 2021; Yang & Zhang 2021; Wang et al. 2022a; Zhang 2022b), see the comprehensive review by Zhang (2022a). These theoretically motivated suggestions are also supported by the results of this work, as will be discussed in Section 5. With two independent detections of FRB 200428 in different wavelength bands by CHIME and STARE2, we find that the spectrum can be fitted as a Gaussian with a narrow characteristic spectral width referenced to the central frequency, $\delta\nu/\nu_0 = 0.278$ (Appendix B). Fig. 2 demonstrates how specific fluence and pulse duration of FRB 200428 change beyond the FRB jet cone, assuming typical values of Γ and θ_j according to the above discussion.

The viewing angle, θ, must not lie too far outside the FRB jet cone so the specific fluence does not drop below the telescope sensitivity threshold. There exists a maximum viewing angle, $\theta_{\max}$, that defines a maximum FRB jet offset angle $\Delta\theta_{\max} = \theta_{\max} - \theta_j$ (see Fig. 1). That is, $\Delta\theta_{\max}$ is the viewing angle beyond the jet cone at which the SRB specific fluence diminishes to the telescope sensitivity threshold, $\mathcal{F}^{\text{SRB}} = \mathcal{F}_{\text{th}}$.

Combining equations 1, 5 and 9, one gets

$$\Delta\theta_{\max} = \cos^{-1}\left[\frac{1 - \mathcal{R}_{\mathcal{D}}(1 - \beta)}{\beta}\right] \quad (11)$$

where $\mathcal{R}_{\mathcal{D}} = w^{\text{SRB}}/w^{\text{FRB}}$ is obtained by numerically solving equation 9 or 10 with $\mathcal{F}^{\text{SRB}} = \mathcal{F}_{\text{th}}$.

In this beaming interpretation, the half opening angle of radio emission, $\theta_{\max} = \Delta\theta_{\max} + \theta_j$, has a maximum value of $\pi/2$. If the FRB jet is geometrically wide ($\theta_j \sim \pi/2$) and/or not highly relativistic ($\Gamma \sim 1$), then radio emission is detectable at all viewing angles, $\theta_{\max} = \pi/2$. The effect is apparent in the upper-left region of the right panel of Fig. 3, where θ_j is large and Γ is small.

Zhang (2021) defines a solid angle ratio between detectable Galactic SRBs and FRBs,

$$\mathcal{R}_{\Delta\Omega} \equiv \frac{\Delta\Omega^{\text{SRB}}}{\Delta\Omega^{\text{FRB}}} \quad (12)$$

where $\Delta\Omega^{\text{SRB}}$ and $\Delta\Omega^{\text{FRB}}$ are the solid angles of the SRB and FRB jet

beam, respectively. Expanding and simplifying $\Delta\Omega^{\text{SRB}}$ and $\Delta\Omega^{\text{FRB}}$,

$$\mathcal{R}_{\Delta\Omega} = \frac{\int_0^{2\pi}\int_{\theta_j}^{\Delta\theta_{\max}+\theta_j}\sin\theta\, d\theta\, d\phi}{\int_0^{2\pi}\int_0^{\theta_j}\sin\theta\, d\theta\, d\phi}$$
$$= \frac{\cos\theta_j - \cos(\Delta\theta_{\max} + \theta_j)}{1 - \cos\theta_j}. \quad (13)$$

In the case where the SRB is detectable at all viewing angles beyond the FRB jet cone, $\Delta\theta_{\max} + \theta_j = \pi/2$, equation 13 simplifies to

$$\mathcal{R}_{\Delta\Omega} = \frac{\cos\theta_j}{1 - \cos\theta_j}. \quad (14)$$

Equation 13 represents the ratio of the detectable region of an SRB to that of an FRB, given certain FRB beaming properties and a particular telescope sensitivity threshold. In this work we consider FAST with a fluence sensitivity threshold of $\mathcal{F}_{\text{th, FAST}} \approx 10$ mJy ms for a 1 ms burst (Lin et al. 2020a; FAST Collaboration et al. 2019).

The solid angle ratio, $\mathcal{R}_{\Delta\Omega}$, is analogous to the ratio of detected SRBs to FRBs from Galactic magnetars. Contours of geometric and relativistic FRB beaming factors for various solid angle ratios are shown in Fig. 3 for a narrow FRB spectrum (*left*: $\delta\nu/\nu \sim 0.1$) and a wide, essentially flat FRB spectrum (*right*: $\delta\nu/\nu \sim 10^3$), where $\delta\nu/\nu$ is the characteristic spectral width of the FRB referenced to the emission frequency. Notice that for any given $\mathcal{R}_{\Delta\Omega}$, FRB beaming is more constrained when the spectrum is narrow versus when it is wide. This suggests that an FRB with a narrow Gaussian spectrum is more sensitive to relativistic beaming effects, i.e., it will undergo a more rapid decline in fluence beyond the FRB beam.

3 RADIO NON-DETECTIONS DURING SGR BURSTING PHASES

Since FRB 200428 was associated with an XRB, we also consider FRB beaming constraints based on non-detections of radio emission concurrent with XRBs. FAST is presently the world's most sensitive radio telescope (see Section 4.2.3), and its extensive monitoring of SGR J1935+2154 provides substantial data to constrain the FRB/SRB–XRB association.

The flux contrast of non-detections should be

$$\frac{F_\nu^{\text{FRB}}}{F_\nu^{\text{th, FAST}}} = \frac{f_\nu^{\text{FRB}}}{f_\nu^{\text{th, FAST}}} \gtrsim \eta = 1.5 \times 10^8 \quad (15)$$

where $f_\nu^{\text{FRB}} \gtrsim 1.5$ MJy ms is the fluence of FRB 200428, and $f_\nu^{\text{th, FAST}} \approx 10$ mJy ms for a 1 ms burst is the fluence sensitivity threshold of FAST. F_ν^{FRB} and $F_\nu^{\text{th, FAST}}$ are the corresponding flux densities (Lin et al. 2020a).

Consider the flux ratio, η, which is identical to the luminosity ratio given the same source, equation 8. We assume that FRB 200428 was viewed on-axis, $\theta < \theta_j$, and that XRB-associated FRBs not detected by FAST have $\theta > \theta_j$, and so

$$\left[\frac{1 - \beta\cos(\Delta\theta)}{1 - \beta}\right]^3$$
$$\times \exp\left\{\frac{1}{2}\left(\frac{\nu_1}{\delta\nu^{\text{on}}}\right)^2\left(\frac{1 - \beta\cos(\Delta\theta)}{1 - \beta}\frac{\nu_2}{\nu_1} - 1\right)^2\right\} \gtrsim \eta. \quad (16)$$

Equation 16 can be numerically solved as an equality to obtain a characteristic viewing angle, $\Delta\theta_c$, so that the above condition will
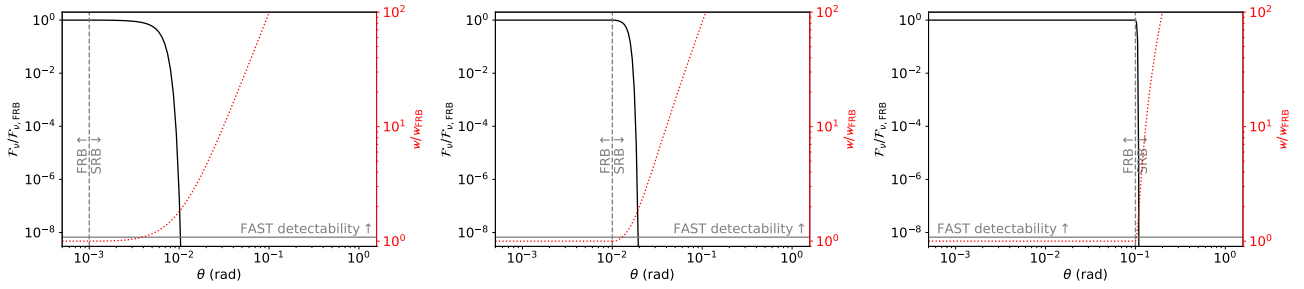
Figure 2. Burst specific fluence (*left axis*) and pulse duration (*right axis*) expressed in terms of on-beam FRB properties ($\mathcal{F}_{FRB}$ = 1.5 MJy ms and w_{FRB} = 0.61 ms for FRB 200428) as a function of viewing angle. The vertical line (*grey, dashed*) represents the presumed geometric width of the FRB beam, θ_j. In each panel, θ_j is varied (*left:* $\theta_j = 10^{-3}$ rad, *middle:* $\theta_j = 10^{-2}$ rad, *right:* $\theta_j = 10^{-1}$ rad) while $\Gamma = 100$ is unchanged. Notice in the left panel that when $\theta_j < 1/\Gamma$, the FRB specific fluence is mostly preserved until $\theta \sim 1/\Gamma$, and conversely in the right panel that when $\theta_j > 1/\Gamma$, the FRB specific fluence drops off very sharply beyond θ_j. The horizontal line (*grey, solid*) represents the FAST sensitivity threshold, above which radio emission is detectable by FAST.
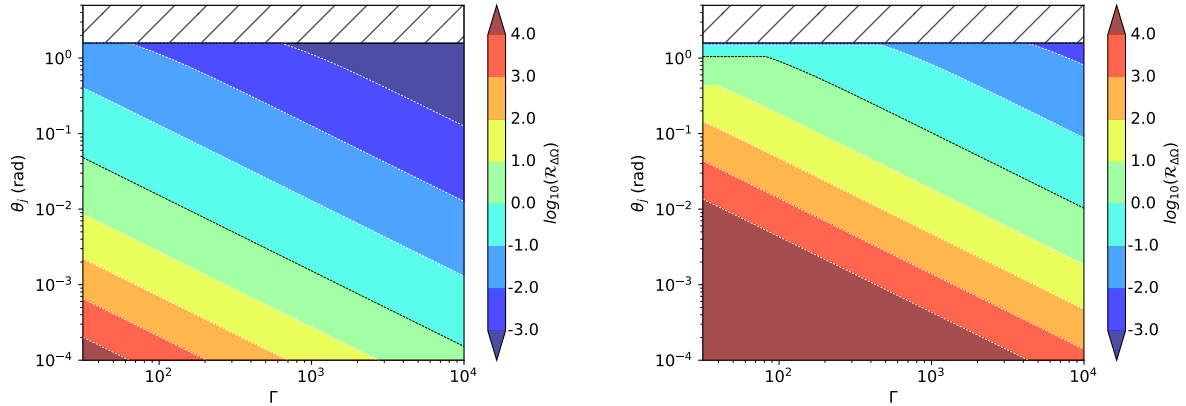
Figure 3. FRB beaming constraints for FRB 200428. The left panel shows the case of a narrow spectrum, $\delta\nu/\nu = 0.1$; the right, a wide (i.e., flat) spectrum, $\delta\nu/\nu = 10^3$. The black dotted line represents $\Omega_{SRB} = \Omega_{FRB}$, or $\mathcal{R}_{\Delta\Omega} = 1$. Constant constraints for the geometric FRB beaming angle, especially apparent FRBs with flat spectra, is due to the off-axis SRBs being visible at all viewing angles, $\theta_{max} = \pi/2$. The hatched region represents the geometrically forbidden and unphysical region of FRB beaming, $\theta_j > \pi/2$.

be satisfied if $\Delta\theta > \Delta\theta_c$. We assume that SGR burst emission is 2π steradians[1] so that the probability for FRB/SRB–XRB associations is

$$P_0 \geq P \simeq \frac{1}{2\pi}\left(2\pi \int_0^{\theta_j + \Delta\theta_c} \sin\theta d\theta\right) = 1 - \cos(\theta_j + \Delta\theta_c). \quad (17)$$

The true probability of FAST detecting an SRB associated with an XRB, P, is probably less than the observed ratio of SRB-associated to SRB-absent XRBs, P_0. Therefore,

$$\theta_j \leq \arccos(1 - P_0) - \Delta\theta_c. \quad (18)$$

Contours of geometric and relativistic FRB beaming factors for various detection probabilities are shown in Fig. 4. In the left panel, the FRB spectrum is assumed to be narrow ($\delta\nu/\nu \sim 0.1$), in the right panel, wide ($\delta\nu/\nu \sim 10^3$). The Lorentz factor is more difficult to constrain for an FRB with a narrow Gaussian spectrum compared to an FRB with a flat spectrum because the former is more sensitive to

relativistic beaming effects compared to the latter. That is, a highly relativistic FRB with a flat spectrum has an off-axis SRB comparable to that of a less relativistic FRB with a narrower spectrum.

4 OBSERVATIONAL DATA

This work incorporates a comprehensive collection of X-ray and radio observations of SGR J1935+2154 conducted by various telescopes in order to obtain well-sampled constraints to FRB beaming. Section 4.1 presents the X-ray observations relevant to this work, namely XRBs detected with associated radio emission and XRBs detected during FAST observing windows wherein no pulsed radio emission was detected. Section 4.2 presents eight radio bursts detected from the source following FRB 200428 and outlines the radio observation epochs conducted by FAST concurrent with 140 XRB detections not associated with pulsed radio emission.

4.1 X-ray observations

On 2020 April 27 UTC 18:26:20, the Swift Burst Alert Telescope (Swift/BAT) and Fermi/GBM were triggered by an active phase of the Galactic magnetar SGR J1935+2154 (Palmer & BAT Team 2020;

---

[1] Lin et al. (2020a) previously provided FRB beaming constraints in this fashion but assumed that the SGR burst emission is isotropic (4π steradians) and that the FRB spectrum is flat (see Extended Data Fig. 4 therein, which is consistent with Fig. 4 right panel).
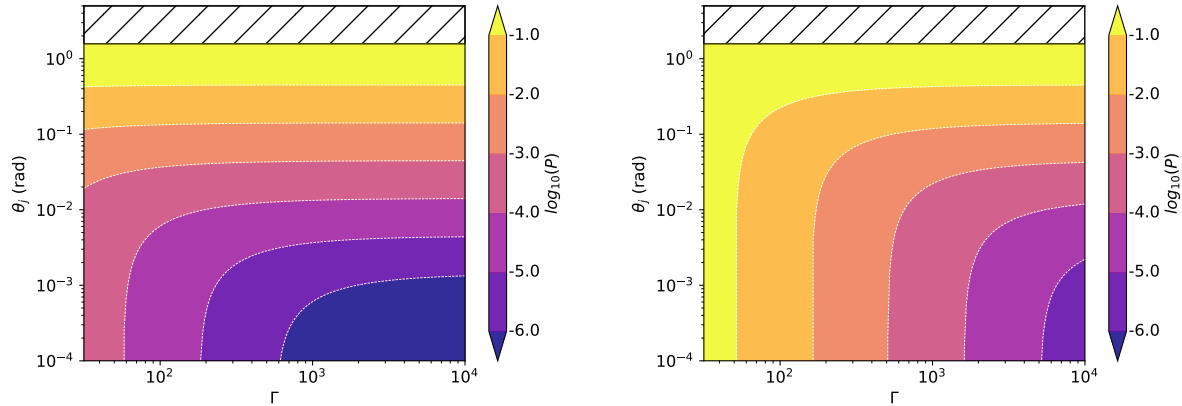
Figure 4. FRB beaming constraints by non-detections of radio emission by FAST concurrent with XRBs for a FRB 200428 reference FRB assuming isotropic XRB emission. The left panel shows the case of a narrow FRB spectrum, $\delta\nu/\nu = 0.1$; the right, a wide (i.e., flat) FRB spectrum, $\delta\nu/\nu = 10^3$. The Lorentz factor is more difficult to constrain for FRBs with narrow Gaussian spectra (*left*) compared to FRBs with flat spectra (*right*). This is because the former is more sensitive to relativistic beaming effects compared to the latter. Notice that geometric beaming is unaffected by the spectral width of the Gaussian FRB. The hatched region represents the forbidden unphysical region of geometric FRB beaming, $\theta_j > \pi/2$.

Fletcher & Fermi GBM Team 2020). Shortly thereafter, a series of X-ray telescopes began target-of-opportunity observations of the source. Throughout the 2020 active bursting phase, only one XRB was detected in association with radio emission (FRB 200428), while 140 XRBs were detected during FAST observing windows wherein no pulsed radio emission was detected.

On 2022 October 10, Swift/BAT and INTEGRAL detected a number of XRBs from SGR J1935+2154 (Palm 2022; Mereghetti et al. 2022), indicating that the magnetar was entering another active bursting phase. In the following weeks, two XRBs were detected (Wang et al. 2022b; Li et al. 2022b), both with arrival times coincident with the detection of radio bursts (Dong & Chime/Frb Collaboration 2022; Huang et al. 2022).

The various X-ray observation campaigns of the source are outlined in this section, and the relevant XRBs are listed in Appendix A.

4.1.1 Fermi/GBM

The Fermi Gamma-ray Space Telescope was launched on 2008 June 11 carrying two scientific instruments, the Large Area Telescope (LAT) and the GBM. The LAT observes gamma-rays above ~20 MeV while the GBM observes gamma-rays between ~8 keV and ~40 MeV (Meegan et al. 2009).

On 2020 27 April at UTC 18:26:20.16, Fermi/GBM triggered on a bright, SGR-like burst from the direction of the magnetar SGR J1935+2154. The burst had a T_{90} duration of ~2 seconds with a fluence of $20 \pm 2 \times 10^{-8}$ erg cm^{-2} s^{-1} in the energy range of 10–200 keV. Fermi/GBM subsequently triggered on multiple bursts from SGR 1935+2154, indicating that the magnetar was entering an active bursting phase (Fletcher & Fermi GBM Team 2020).

Lin et al. (2020a) reported no pulsed radio emission from SGR J1935+2154 detected in association with 29 XRBs detected by Fermi/GBM (see also Zou et al. 2021). More recently, Yang et al. (2021) performed a thorough untriggered burst search on Fermi/GBM data to identify 34 radio-absent XRBs during the same FAST observing session between 2020 April 27 UTC 23:55:00 and 2020 28 April 00:50:37. Continuous Fermi/GBM data from 2013 January to 2021 October reveals no additional XRB detections dur-

ing FAST observing sessions through 2020 October (Lin et al. 2020b; Zhu et al. 2022). In this work we include 34 XRBs from SGR J1935+2154 detected by Fermi/GBM during simultaneous monitoring by FAST, based on the more recent untriggered burst search in Yang et al. (2021).

4.1.2 Insight–HXMT

The Insight Hard X-ray Modulation Telescope (HXMT) is China's first astronomical satellite launched on 2017 June 15. It contains three detectors for low-, medium- and high- energy emission with a total energy range of 1–250 keV. (Zhang et al. 2018).

After Swift/BAT and Fermi/GBM alerted that SGR J1935+2154 was entering a new active bursting phase, Insight–HXMT began observing SGR J1935+2154 and detected 11 bursts within a total of 17 hours. The brightest burst was detected on 2020 April 28 at a geocentric arrival time of UTC 14:34:24.0114, less than a second before FRB 200428 was detected by CHIME and STARE2. All three X-ray telescopes aboard Insight–HXMT detected the burst with a combined fluence of $63.68 \pm 6.62 \times 10^{-8}$ erg cm^{-2} s^{-1} in the energy range of 1–250 keV, and a duration of 0.53 s (Li et al. 2021).

Data catalogs of an Insight–HXMT extended 33-day observation of SGR J1935+2154 beginning on 2020 April 28 reports the detection of two XRBs during simultaneous monitoring of the source by FAST. The detections occurred on 2020 May 6 UTC 22:48:21.550 and 2020 May 12 UTC 21:47:43.340 (Cai et al. 2022a). FAST detected no radio emission concurrent with the detection times.

Since SGR J1935+2154 re-entered an active bursting phase in 2022 October, Insight-HXMT has been observing SGR J1935+2154 since 13 UTC 04:51:43. On 2022 October 21, Insight–HXMT detected an XRB associated with a radio burst detected by the Yunnan 40-meter telescope. When corrected for frequency-dependent dispersion delay, the X-ray arrival time of UTC 10:01:45 is temporally coincident with the radio arrival time (Li et al. 2022b).

4.1.3 NICER

NICER was launched on 2017 June 3 to be fitted as an external attached payload on the International Space Station (ISS). NICER's sole science instrument, the X-ray Timing Instrument (XTI), is a non-imaging soft X-ray (0.2–12 keV) timing and spectroscopy instrument consisting of 56 optical modules that altogether provide an effective area of nearly 2,500 cm^2 at 1.5 keV (Gendreau et al. 2016).

NICER began observing SGR J1935+2154 on 2020 April 28 UTC 00:40:58, 6 hrs after the initial Swift/BAT and Fermi/GBM triggers that signaled the start of an active bursting phase, and just under 14 hrs prior to FRB 200428. During the first 1120 s, NICER detected over 217 bursts during a highly active burst storm before the detection rate dropped by a factor of over 25 and remained comparatively low thereafter. During the first ~600 seconds of observations while FAST was simultaneously monitoring SGR J1935+2154, NICER detected 137 bursts, 104 of which were unique from the Fermi/GBM detections (Younes et al. 2020).

4.1.4 GECAM

The Gravitational Wave High-energy Electromagnetic Counterpart All-sky Monitor (GECAM) is a pair of satellites developed by the Chinese Academy of Science launched on December 10, 2020. The two satellites are located on opposite sides of the Earth in order to get a simultaneous view of the entire sky. They have identical on-board instrumentation consisting of gamma-ray and charged particle detectors. GECAM's primary mission goal is to find and monitor gamma radiation from gravitational wave event sources, but it will also monitor a variety of other high-energy transients.

On 2020 October 14 UTC 19:21:39.100, GECAM detected an XRB from SGR J1935+2154 at a de-dispersed arrival time consistent with a radio burst detected by CHIME. The in-flight and ground localization given by both instruments is consistent with SGR J1935+2154 within error (Wang et al. 2022b).

4.2 Radio observations

In the months following FRB 200428, many radio telescopes monitored SGR J1935+2154 but most observation campaigns led to null results. The few successful radio detections from SGR J1935+2154 in 2020 all appeared much weaker (and most slower) than FRB 200428.

On 2022 October 10, Swift/BAT and INTEGRAL detected a number of XRBs from SGR J1935+2154 (Palm 2022; Mereghetti et al. 2022), indicating that the magnetar was entering another active bursting phase. In the following weeks, two radio bursts were detected (Dong & Chime/Frb Collaboration 2022; Huang et al. 2022), both with arrival times coincident with the detection of XRBs ((Wang et al. 2022b; Li et al. 2022b)).

This section presents the detections of radio bursts from SGR J1935+2154, and their properties are listed in Table 1.

4.2.1 STARE2

The STARE2 is a network of three 1281–1468 MHz radio telescopes in the southwestern United States with a field-of-view of 3.6 steradians and a sensitivity threshold of 1 ms above ~300 kJy (Bochenek et al. 2020a).

All three STARE2 detectors were triggered at a geocentric arrival time referenced to infinite frequency of 2020 April 28 UTC 14:34:24.45548. The event, since referred to as FRB 200428, had a band-averaged fluence of 1.5 MJy ms with an effective frequency of

1,378 MHz, a FWHM temporal duration of 0.61 ms, and dispersion measure (DM) of 332.702 pc cm^{-3}. The STARE2 detection was temporally coincident and had a similar DM with the event detected by CHIME (discussed in Section 4.2.2), but with approximately 1,000 times higher fluence. (Bochenek et al. 2020b).

4.2.2 CHIME

The CHIME is a radio telescope consisting of four fixed reflecting cylinders, each with 256 equispaced antennas sensitive to 400–800 MHz radiation, altogether providing a field-of-view of at least 200 deg^2 (Newburgh et al. 2014). Originally conceived to map baryon acoustic oscillation features in redshifted hydrogen, its large field-of-view and collecting area, wide radio bandwidth, and primary beam consisting of 1024 individual beams, make it an ideal detector of FRBs (The CHIME/FRB Collaboration et al. 2018).

On 2020 April 28, CHIME detected a dispersed radio burst consisting of two independent sub-bursts at geocentric arrival times referenced to infinite frequency of 14:34:24.42650(2) and 14:34:24.45547(2). The 400–800 MHz averaged fluences were 480 kJy ms and 220 kJy ms, and the temporal widths (after correcting for propagation and beam-attenuation effects) were 0.585 ± 0.014 ms and 0.335 ± 0.007 ms, respectively. The two burst components, fitted jointly, have a dispersion measure (DM) of 332.7206(9). The values in parentheses denote uncertainties of a 68.3% confidence interval in the last significant digit (The CHIME/FRB Collaboration 2020). The second component of the CHIME burst is the lower-frequency component of the STARE2 burst since the geocentric arrival times referenced to infinite frequency are temporally consistent between the two (Bochenek et al. 2020b).

On 2020 October 8, CHIME detected three more radio pulses from SGR J1935+2154. The pulses were detected at UTC 02:23:41.976, 02:23:43.922 and 02:23:44.871 at the CHIME location at a frequency of 400.195 MHz. The 400–800 MHz fluences were 900 ± 160, 9.2 ± 1.6 and 6.4 ± 1.1 Jy ms. Only the first and brightest burst was fitted to obtain a DM of 332.658 ± 0.002 pc cm^{-3} and an intrinsic width of 0.26 ± 0.01 ms (Pleunis & CHIME/FRB Collaboration 2020).

4.2.3 FAST

FAST is located in a radio-quiet region in southwest China and is the world's largest and most sensitive radio telescope with an illuminated aperture of 300 m. The dish can achieve sky coverage of a zenith angle up to 40° and observe across a wide frequency band of 70 MHz–3 GHz using an ultra-wideband receiver or 1.05 - 1.45 GHz using a highly sensitive 19-beam receiver (Nan et al. 2011). The fluence threshold of FAST is ≈ 10 mJy ms for a 1 ms burst, several orders of magnitude lower than any other radio telescope in operation as of 2022 (Lin et al. 2020a).

FAST was observing SGR J1935+2154 since 2020 April 15 and began an extended observation campaign from April 28 to May 19 with a total duration of 26 hours (Zhu et al. 2022). Unfortunately FAST was not observing SGR J1935+2154 at the time of FRB 200428. On 2020 April 30, FAST detected a highly polarized radio burst from the source at UTC 21:43:00.42 (MJD 58969.9048669008). The 19-beam receiver was mounted on the telescope for observations at a central frequency of 1.25 GHz with a bandwidth of 460 MHz. The burst fluence was 60 mJy ms with a duration of 1.966 ms and the DM was 332.9 pc cm^{-3} (Zhang et al. 2020). This event had far weaker fluence than any other radio signal from the source by several orders of magnitude, yet was still detected

Table 1. Radio detections from SGR J1935+2154. The first three entries are independent detections of FRB 200428. For completeness, the two sub-bursts of the CHIME detection are listed separately.

Telescope	Date	Time (UTC)	Fluence	FWHM (ms)	DM (pc cm^{-3})	$\nu_0^{\S}$
CHIME[†]	2020 April 28	14:34:24.42650	480 kJy ms[‡]	0.585 ± 0.014 ms	332.7 ± 0.0009	600 MHz
CHIME[†]	2020 April 28	14:34:24.45547	220 kJy ms[‡]	0.335 ± 0.007 ms	332.7 ± 0.0009	600 MHz
STARE2[†]	2020 April 28	14:34:24.45548	1.5 ± 0.3 MJy ms	0.61 ± 0.09 ms	332.7 ± 0.008	1378 MHz
FAST	2020 April 30	22:20:00	60 mJy ms[*]	0.93 ms[*]	332.9[*]	1250 MHz
Westerbork	2020 May 24	22:19:19.67464	112 ± 22 Jy ms	0.427 ± 0.033 ms	332.9 ± 0.21	1324 MHz
Westerbork	2020 May 24	22:19:21.07058	24 ± 5 Jy ms	0.219 ± 0.027 ms	332.9 ± 0.21	1324 MHz
MNC	2020 May 30	00:31:03	457 mJy ms[*]	114.174 ms[*]	316.0 ± 17.5	408 MHz
BSA/LPI	2020 September 2	18:14:59	47.6 Jy ms[*]	340 ms[*]	320.0 ± 10	111 MHz
CHIME	2020 October 8	02:23:41.976	900 ± 160 Jy ms	0.26 ± 0.01 ms	332.7 ± 0.002	600 MHz
CHIME	2022 October 14	19:21:47	20 kJy ms[*]	13 ms[*]	332.8 ± 0.4	600 MHz
Yunnan	2022 October 21	10:01:45.84215	15 Jy ms	0.75 ms[*]	313[*]	2245 MHz

[§] Central observing frequency.
[†] These radio detections are collectively defined as FRB 200428.
[‡] Detection far outside the primary-beam main lobe introduces uncertainty of a factor of two (The CHIME/FRB Collaboration 2020).
[*] Uncertainties are not reported for these quantities.

with a signal-to-noise ratio (SNR) of 1092. In the months after May, FAST stopped monitoring SGR J1935+2154 due to a lack of radio activity. In August, FAST returned twice to observe the source but did not detect any radio emission (Zhu et al. 2022). In October, FAST detected periodic radio pulses from the source, $P \approx 3.248$ s, with fluences up to 40 mJy ms (Zhu et al. 2020).

4.2.4 Westerbork RT1

Originally constructed in Netherlands in the 1960s, the Westerbork Synthesis Radio Telescope (WSRT) consists of 10 polar mounted reflector antennas each with a 25 m diameter, placed at an interval of 144 m along an east–west baseline. A 300 m long rail track at the eastern end carries two additional mobile antennas. 1.4 km to the east lies two more antennas placed on movable rails for a total of 14 identical radio antennas (Baars et al. 2019).

Since the announcement of FRB 200428, the single 25 m dish RT1 was used alongside the 25 m and 20 m telescopes at Onsala Space Observatory in Sweden and the 32 m dish in Toruń, Poland to observe SGR J1935+2154. Between 2020 April 29 and 2020 July 27 the group of telescopes observed the source for a total on-source time of 522.7 hours. Westerbork RT1 detected two bursts at barycentric arrival times referenced to infinite frequency of UTC 22:19:19.67464 and 22:19:21.07058. The two bursts were detected at a central observing frequency of 1,324 MHz and bandwidth of 128 MHz with fluences of 112 ± 22 and 24 ± 5 and pulse widths of 427 ± 33 and 219 ± 27, respectively. The DM of the bursts were calculated to be 332.85 ± 0.21 pc cm^{-3} and 332.94 ± 0.21 pc cm^{-3}, respectively (Kirsten et al. 2021).

4.2.5 Medicina Northern Cross

The Northern Cross at the Medicina Radio Astronomical Station (or Medicina Northern Cross; MNC) located in Bologna, Italy, is a T-shaped interferometer operating at a frequency of 408 MHz with a 16 MHz bandwitdh. The north-south arm recently underwent refurbishment for use in the search for FRBs (Locatelli et al. 2020).

Beginning on 2020 April 30, MNC monitored SGR J1935+2154 almost daily for up to 1.5 hours. On 2020 May 30, MNC detected periodic radio pulsations from the source with a SNR of 6.8. The flux

density was inferred to be 4 mJy and the pulse width was measured to be 114.174 ms, implying a fluence of 457 mJy ms. The DM was calculated to be 316.011 ± 17.526 pc cm^{-3} (Burgay et al. 2020).

4.2.6 BSA/LPI

The Big Scanning Array of Lebedev Physical Institute (BSA/LPI), located in Puschino, Russia, is a phased antenna array operating at a central observing frequency of 111 MHz with a bandwith of 2.5 MHz (Tyul'bashev et al. 2016). The team carried out a search of radio pulses from SGR J1935+2154 on observational data spanning 2020 January 1 to 2020 November 16, totaling approximately 26 hours of observations. They found a single pulse registered on 2020 September 2 at UTC 18:14:59 with a flux density of 140 mJy and pulse width of 2.2 s, corresponding to a fluence of ~308 Jy ms. The burst was detected with a SNR of 6.6 and the DM was calculated to be 320 ± 10 pc cm^{-3}. The pulse arrival time indicated that the signal landed on the side lobe of the BSA LPI beam, so the flux density represents a lower limit (Alexander & Fedorova 2020).

4.2.7 Yunnan Astronomical Observatory

Triggered by renewed bursting activity from SGR J1935+2154 in 2022 October, The 40-meter radio telescope at the Yunnan Astronomical Observatory in southwest China detected a radio burst on 2022 October 21 UTC 10:01:45.84215. The signal was detected at a central frequency of 2.245 GHz and frequency bandwidth of 110 MHz, with a detection significance of 20σ. The estimated flux and fluence of the burst are 20 Jy and 15 Jy ms, respectively. The best estimation for the DM is 313 pc cm^{-3}, which is significantly lower than previously reported detections, which indicates a dynamically evolving environment (Huang et al. 2022).

5 RESULTS AND DISCUSSION

The radio detections from SGR J1935+2154 (Table 1) span a period of approximately 5 months during an active bursting phase of the Galactic magnetar wherein several radio pulses have been detected. The fast radio burst on 2020 April 28 (FRB 200428) was detected by
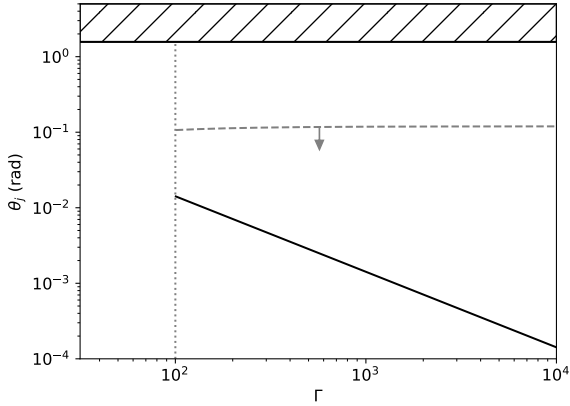
Figure 5. Observational beaming constraints of FRBs from the Galactic magnetar SGR J1935+2154. The main constraint (*solid, black*) is obtained from the detection of two SRBs and one FRB from the source ($\mathcal{R}_{\Delta\Omega} = 2$). An upper limit constraint (*dashed, black*) is obtained by non-detections of radio emission by FAST concurrent with 140 XRBs, where every XRB is assumed to be intrinsically associated with an SRB ($f_{FRB} = 1$). Note that the main constraint is consistent with the upper limit. If not every XRB is assumed to be intrinsically associated with an SRB ($f_{FRB} < 1$), the upper limit is raised further and remains consistent with the main constraint.

both CHIME and STARE2 with fluence values many orders of magnitude greater than any radio signal ever detected. CHIME detected two components separated by 29 ms, where the second component is temporally coincident with the STARE2 detection. These three independent signals are collectively identified as FRB 200428. For completeness they are included in Table 1.

Given two independent detections of FRB 200428 in different wavelength bands, and assuming the burst is of Gaussian spectral shape, one obtains a characteristic burst spectral width of FRB 200428 referenced to its central frequency, $\delta\nu_{FRB}/\nu_{0,FRB} = 0.278$ (Appendix B).

FRB 200428 was detected in association with an XRB. We therefore initially hypothesize that all SRBs are similarly associated with XRBs.

However, some radio bursts were detected with an associated XRB while most were not. During the 2020 active bursting phase of SGR J1935+2154, no radio pulse besides FRB 200428 was detected with an associated XRB. Furthermore, they were detected with much lower fluences and longer durations than FRB 200428. Meanwhile, in 2020, FAST detected no pulsed radio emission from the source concurrent with 140 XRBs before and after FRB 200428. During the 2022 active bursting phase, two radio pulses were detected with associated XRBs. We use these observational facts to constrain FRB beaming under our first hypothesis.

5.1 XRB-associated SRBs

A total of three radio pulses have been detected in association with XRBs: FRB 200428 in 2020 and the two radio pulses in 2022. The two radio pulses in 2022 had much weaker fluence and longer duration than FRB 200428, suggesting they might be SRBs. We use the FRB–SRB closure relation of equation 9 with a reference FRB identical to FRB 200428 (hereafter "reference FRB-1"). For the CHIME radio detection on 2022 October 14 there is no solution, meaning that it cannot be an SRB of a reference FRB-1 with a Gaussian-like

spectrum. We instead use the power-law closure relation derived in Zhang (2021) to find that the CHIME detection on 2022 October 14 may indeed be an SRB of a reference FRB-1 with a power-law spectrum of index $\alpha = -0.8$. For the Yunnan radio detection on 2022 October 21, we find that it may be an SRB of a reference FRB-1 with a Gaussian spectrum of narrow characteristic width, $\delta\nu/\nu = 0.16$.

The detection of two SRBs and one FRB from SGR J1935+2154 implies that the ratio of solid angles between SRBs and FRBs is $\mathcal{R}_{\Delta\Omega} \sim 2$. Equation 13 represents how the solid angle ratio depends on geometric and relativistic FRB beaming factors, which is used to constrain observations. The observational constraints are given in Fig. 5. We find that FRB beaming must be geometrically narrow and that the beaming factors follow $\theta_j\Gamma \sim 2$.

An additional constraint on FRB beaming is imposed by the non-detections of radio emission by FAST concurrent with 140 XRBs. We assign an upper limit for FAST detecting an FRB associated with an XRB as $P \leq 1/141$. This upper-limit constraint is consistent with the main constraint. Theoretical descriptions of FRBs derive that the emission is highly relativistic, $\Gamma \gtrsim 10^2$ (Lyubarsky 2008; Murase et al. 2016; Lu & Kumar 2018; Zhang 2022b), see Zhang (2022a) for a review. We additionally constrain the relativistic beaming factor to be $\Gamma \geq 10^2$.

5.1.1 On the possible uniqueness of SRB-associated XRBs

During its 2020 observation campaigns of SGR J1935+2154, FAST detected no radio emission concurrent with 140 XRBs. The utter lack of radio detections by the highly sensitive FAST challenges the assumption that all XRBs are intrinsically associated with SRBs. Furthermore, recent studies suggest that the XRB associated with FRB 200428 was intrinsically unique from the majority (Younes et al. 2021; Yang et al. 2021; Li et al. 2022a). We consider the possibility that not all XRBs are intrinsically associated with SRBs by introducing a free parameter, $f_{FRB} \leq 1$, that represents the fraction of XRBs that are intrinsically associated with FRBs (SRBs). If all SGR bursts that produce XRBs also produce FRBs, $f_{FRB} = 1$, and the earlier constraints are unchanged. On the other hand, if not all XRBs are intrinsically associated with FRBs, $f_{FRB} < 1$.

In this work we consider the limiting case of $f_{FRB} = 1/141$ based on observations by FAST. While we now assume that one out of 141 XRBs are intrinsically associated with FRBs, we still assume that all FRBs (SRBs) are associated with XRBs. That is, the relationship between FRBs and SRBs is unaffected by f_{FRB} since both are equally subject to the added constraint, and so $\mathcal{R}_{\Delta\Omega}$ is unchanged. The FRB beaming constraint by non-detections of radio emission by FAST concurrent with XRBs (see Fig. 5) becomes $P \leq 1/(141 \times f_{FRB}) = 1$ and the geometric constraint is loosened to the maximum value, $\theta_j = \pi/2$. This is expected since the introduction of $f_{FRB} < 1$ ascribes the observational scarcity to more than just beaming (i.e., intrinsic factors) so that constraints by beaming alone must be weaker. We note that regardless of the value of f_{FRB}, the upper-limit constraint for FRB beaming remains consistent with the main constraint.

5.2 XRB-independent SRBs

In our second hypothesis we eliminate the requirement that SRBs must be associated with XRBs. We again use the FRB–SRB closure relation in equation 9 to determine whether any of the subsequent radio detections are SRBs. We first consider a reference FRB identical to FRB 200428 ("reference FRB-1").

Table 2. SRBs of SGR J1935+2154 by solution of the FRB–SRB closure relation. Bolded entries denote SRBs detected in associated with an XRB.

Reference FRB	Scope	Date	Time (UTC)	$\delta\nu/\nu^{\dagger}$	$\alpha^{\ddagger}$
FRB 200428	FAST	2020 April 30	21:43:00.42	0.36	—
	BSA/LPI	2020 September 2	18:14:59	—	-1.1
	Yunnan	**2022 October 21**	**10:01:45.84215**	**0.16**	—
Short-Duration Cosmological FRB	Westerbork	2020 May 24	22:19:19.67464	0.80	—
	Westerbork	2020 May 24	22:19:21.07058	0.27	—
	CHIME	2020 October 8	02:23:41.976	0.068	—
	CHIME	**2022 October 14**	**19:21:47**	—	**-0.8**

† Gaussian spectral width referenced to peak of the associated FRB.
‡ Power-law index of the associated FRB.

5.2.1 SRBs of FRB 200428

The MNC detection satisfies the FRB–SRB closure relation with reference FRB-1 if the FRB has a wide spectrum, $\delta\nu/\nu = 15$. There is no solution found for the BSA/LPI detection, meaning that it cannot be an SRB of reference FRB-1 if the FRB spectrum is a Gaussian. Zhang (2021) showed that the burst detected by BSA/LPI can be an SRB of reference FRB-1 only if the FRB spectrum is a power-law of index $\alpha = -1.1$. The highly polarized burst detected by FAST on 2020 April 30 can be an SRB of reference FRB-1 if the FRB has a narrow spectral width, $\delta\nu/\nu = 0.36$. The burst detected by the Yunnan Observatory can be an SRB of reference FRB-1 if the FRB has a narrow spectral width, $\delta\nu/\nu = 0.16$. These SRBs are listed in Table 2.

One would expect that the FRB spectral shape is generally consistent between a population of FRBs from the same source. We note that the average spectral width of reference FRB-1 required by the observed SRBs, $\delta\nu/\nu = 0.26$, is roughly consistent with the characteristic spectral width of FRB 200428 itself, $\delta\nu/\nu = 0.278$ (Appendix B). On the contrary, the BSA/LPI burst may be an SRB of reference FRB-1 only if the FRB has a power-law spectrum. We attribute the inconsistencies in spectral shape to intrinsic factors that are not addressed here. We note that such behavior is observed in the FRB population as a whole, with broad- and narrow-band spectra being regularly observed (e.g., Aggarwal et al. 2021; Pleunis & CHIME/FRB Collaboration 2020), even among different bursts for the same source (Zhou et al. 2022).

The MNC "burst" was in fact a marginal detection of radio pulsations rather than a single bursting event (Burgay et al. 2020). Furthermore, all potential SRBs discussed in this work require their reference FRB to have either a narrow Gaussian spectrum with $\delta\nu/\nu < 1$ or power-law spectrum with $\alpha \sim -1$; only the MNC burst demands legitimacy as an SRB of reference FRB-1 with a wide Gaussian spectrum. For these reasons we exclude the MNC burst from consideration as an SRB.

5.2.2 SRBs of a short-duration cosmological FRB

There have been several radio detections from SGR J1935+2154 with shorter duration than FRB 200428. By definition, these radio pulses cannot be SRBs of reference FRB-1. It is instead possible that they may be SRBs of a different reference FRB. In this section we consider a short-duration cosmological reference FRB, $\mathcal{F}_{\nu} = 100$ MJy ms and $w = 0.1$ ms (hereafter "reference FRB-2").

The two radio detections by Westerbork on 2020 May 24 UTC 22:19:19 and 22:19:21 may both be SRBs of reference FRB-2 if the FRBs have narrow Gaussian spectra, $\delta\nu/\nu = 0.80$ and $\delta\nu/\nu =$ 0.27, respectively. The CHIME detection on 2020 October 8 may be an SRB of reference FRB-2 if the FRB has a narrower Gaussian spectrum, $\delta\nu/\nu = 0.068$. The CHIME detection on 2022 October 14 may be an SRB of reference FRB-2 if the FRB has a power-law spectrum, $\alpha = -0.8$. These SRBs are listed in Table 2.

As with reference FRB-1, we again distinguish between SRBs based on the required spectral shape of reference FRB-2. The three radio detections in 2020 all require that reference FRB-2 has a narrow Gaussian spectrum. We note without statistical justification that the mean spectral width of reference FRB-2 required by these SRBs, $\delta\nu/\nu = 0.38$, is roughly consistent with the characteristic spectral width of FRB 200428 itself, $\delta\nu/\nu = 0.278$ (Appendix B), as well as the average spectral width of reference FRB-1 required by the SRBs detected by FAST and Yunnan Observatory, $\delta\nu/\nu = 0.26$. The power-law SRB detected by CHIME on 2022 October 14 is thus distinguished from the three Gaussian SRBs detected in 2020, as in the case of the BSA/LPI burst and reference FRB-1.

We note that the three bursts discussed in Section 5.2.1 can also be SRBs of reference FRB-2 solely due to their longer duration. Then, the spectra of reference FRB-2 must be very wide, $\delta\nu/\nu = 3.5$ and $\delta\nu/\nu = 2.3$ for the FAST and Yunnan Observatories detections, respectively. We deem it unnecessary to consider reference FRB-2 instead of reference FRB-1 in these cases for two reasons. First, one should expect FRBs from a Galactic magnetar to be similar to FRB 200428 (i.e., not as bright as a cosmological FRB). Second, the spectral widths obtained by using reference FRB-1 are more consistent with the majority of FRBs and SRBs discussed.

5.2.3 FRB beaming constraints

Under our second hypothesis we obtain a total of seven SRBs, five of which were not detected with an associated XRB. All SRBs are listed in table 2 along with the spectral parameters of their reference FRBs obtained from the FRB–SRB closure relations. Three SRBs are found to be related to a reference FRB identical to FRB 200428, two of which require it has a narrow Gaussian spectrum. Considering only the SRBs of FRBs with Gaussian spectra, $\mathcal{R}_{\Delta\Omega} = 2$. The solid line in Fig. 6 shows the geometric and relativistic beaming constraints for reference FRB-1 given a Gaussian spectral width equal to the average required by the two related SRBs, $\delta\nu/\nu = 0.26$.

Meanwhile, four SRBs are found to be related to a short-duration cosmological reference FRB, three of which require that it has a narrow Gaussian spectrum. Considering only the SRBs of FRBs with Gaussian spectra, $\mathcal{R}_{\Delta\Omega} = 3$. The dashed line in Fig. 6 shows the geometric and relativistic beaming constraints for reference FRB-2
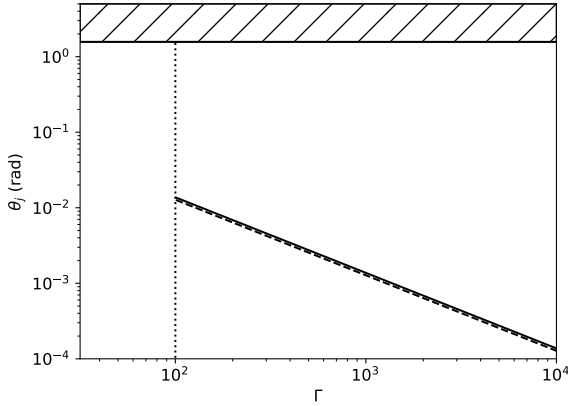
Figure 6. Observational beaming constraints of FRBs from the Galactic magnetar SGR J1935+2154. For reference FRB-1 with a Gaussian spectrum ($\delta\nu/\nu = 0.26$), there are two associated SRBs, $\mathcal{R}_{\Delta\Omega} = 2$ (*solid*). For reference FRB-2 with a Gaussian spectrum ($\delta\nu/\nu = 0.38$), there are three associated SRBs, $\mathcal{R}_{\Delta\Omega} = 3$ (*dashed*). The hatched region represents the geometrically forbidden and unphysical region of FRB beaming, $\theta_j > \pi/2$. The dotted vertical line indicates the theoretical relativistic lower limit of FRBs, $\Gamma \gtrsim 10^2$.

given a Gaussian spectral width equal to the average required by the three related SRBs, $\delta\nu/\nu = 0.38$.

The derived beaming constraints for the two reference FRBs are nearly identical. This coincidence is largely due to $\mathcal{R}_{\Delta\Omega}$ being of order unity for either reference FRB, but is more precisely due to the particular properties of each reference FRB (i.e., fluence, pulse duration, Gaussian spectral width). We find that the geometric and relativistic beaming factors for both reference FRBs follow $\theta_j \Gamma \sim 2$. As more Galactic SRBs and FRBs are detected, $\mathcal{R}_{\Delta\Omega}$ will fluctuate and converge on the physically accurate solid angle ratio between SRBs and FRBs.

6 CONCLUSIONS

In this work we extended theoretical models to constrain geometric and relativistic beaming factors of FRBs with Gaussian spectra and developed computer code to numerically solve the equations. Our results indicate that FRBs with narrow Gaussian spectra are more difficult to geometrically and relativistically constrain. This is due to the fact that narrow spectra are more sensitive to relativistic effects versus wide FRB spectra. We provided observational constraints under two separate hypotheses.

In the first we assumed that SRBs are associated with XRBs like the case of FRB 200428 and find a total of two SRBs. We constrain FRB beaming to be geometrically narrow and highly relativistic, with combined beaming factors that follow $\theta_j \Gamma \sim 2$.

The observational scarcity of FRBs associated with XRBs, along with findings from recent studies, suggest that the XRB associated with FRB 200428 was intrinsically unique. We investigated how the beaming interpretation is affected by this uncertainty by introducing the free parameter, $f_{\rm FRB}$ to represent the fraction of XRBs that are intrinsically associated with FRBs. We note that $f_{\rm FRB}$ only affects the constraint obtained by non-detections of radio emission by FAST concurrent with XRBs. As radio-burst-associated XRBs are considered increasingly rare, $f_{\rm FRB} < 1$, the geometric constraint on FRB beaming is increasingly loosened. At a reference limit of

$f_{\rm FRB} = 1/141$, the geometric constraint is loosened to the maximum value, $\theta_j = \pi/2$. We confirmed that for any value of $f_{\rm FRB}$, the upper-limit constraint on FRB beaming remains consistent with the main constraint.

In our second hypothesis we forgo the stringent requirement that all SRBs are associated with XRBs. We find an additional five potential SRBs from SGR J1935+2154 for a grand total of seven SRBs from the Galactic magnetar. Until a considerable number of additional detections are successful, $\mathcal{R}_{\Delta\Omega} \sim 2$ and FRB beaming factors will follow $\theta_j \Gamma \sim 2$.

Regardless of whether FRBs and SRBs are intrinsically associated with XRBs, our results under both hypotheses show that FRB beaming is geometrically narrow and highly relativistic. This fact is consistent with theoretical models for FRBs that support a magnetospheric origin of emission (Kumar et al. 2017; Yang & Zhang 2018; Metzger et al. 2019; Wadiasingh & Timokhin 2019; Wang et al. 2020; Kumar & Bošnjak 2020; Lu et al. 2020; Yang et al. 2020; Wadiasingh et al. 2020; Qu & Zhang 2021; Yang & Zhang 2021; Wang et al. 2022a; Zhang 2022b). Further FRB, SRB and XRB detections from SGR J1935+2154 will continually improve constraints on FRB beaming until statistically precise values can be established.

DATA AVAILABILITY

The Python code developed to perform calculations as part of this work is available upon request.

REFERENCES

Aggarwal K., Agarwal D., Lewis E. F., Anna-Thomas R., Tremblay J. C., Burke-Spolaor S., McLaughlin M. A., Lorimer D. R., 2021, ApJ, 922, 115
Alexander R., Fedorova V., 2020, The Astronomer's Telegram, 14186, 1
Baars J., Buiter J., Kiers R., 2019, in Proceedings of Westerbork Telescope 50th Anniversary — PoS(Westerbork). Sissa Medialab, Westerbork, The Netherlands, p. 003, doi:10.22323/1.361.0003, https://pos.sissa.it/361/003
Bochenek C. D., McKenna D. L., Belov K. V., Kocz J., Kulkarni S. R., Lamb J., Ravi V., Woody D., 2020a, PASP, 132, 034202
Bochenek C. D., Ravi V., Belov K. V., Hallinan G., Kocz J., Kulkarni S. R., McKenna D. L., 2020b, Nature, 587, 59
Burgay M., et al., 2020, The Astronomer's Telegram, 13783, 1
Cai C., et al., 2022a, ApJS, 260, 24
Cai C., et al., 2022b, ApJS, 260, 25
Dong F. A., Chime/Frb Collaboration 2022, The Astronomer's Telegram, 15681, 1
FAST Collaboration et al., 2019, Sci. China Phys. Mech. Astron., 62, 959502
Fletcher C., Fermi GBM Team 2020, GRB Coordinates Network, 27659, 1
Gendreau K. C., et al., 2016, in den Herder J.-W. A., Takahashi T., Bautz M., eds, Society of Photo-Optical Instrumentation Engineers (SPIE) Conference Series Vol. 9905, Space Telescopes and Instrumentation 2016: Ultraviolet to Gamma Ray. p. 99051H, doi:10.1117/12.2231304
Good D., Chime/Frb Collaboration 2020, The Astronomer's Telegram, 14074, 1
Huang Y. X., et al., 2022, The Astronomer's Telegram, 15707, 1
Kirsten F., Snelders M. P., Jenkins M., Nimmo K., van den Eijnden J., Hessels J. W. T., Gawroński M. P., Yang J., 2021, Nat Astron, 5, 414

Kumar P., Bošnjak Ž., 2020, Monthly Notices of the Royal Astronomical Society, 494, 2385

Kumar P., Lu W., Bhattacharya M., 2017, MNRAS, 468, 2726

Li C. K., et al., 2021, Nat Astron, 5, 378

Li X., et al., 2022a, ApJ, 931, 56

Li X. B., et al., 2022b, The Astronomer's Telegram, 15708, 1

Lin L., et al., 2020a, Nature, 587, 63

Lin L., Göğüş E., Roberts O. J., Baring M. G., Kouveliotou C., Kaneko Y., van der Horst A. J., Younes G., 2020b, ApJ, 902, L43

Locatelli N. T., et al., 2020, Monthly Notices of the Royal Astronomical Society, 494, 1229

Lu W., Kumar P., 2018, Monthly Notices of the Royal Astronomical Society, 477, 2470

Lu W., Kumar P., Zhang B., 2020, Monthly Notices of the Royal Astronomical Society, 498, 1397

Lyubarsky Y., 2008, ApJ, 682, 1443

Meegan C., et al., 2009, ApJ, 702, 791

Mereghetti S., et al., 2020, ApJ, 898, L29

Mereghetti S., Gotz D., Ferrigno C., Bozzo E., Savchenko V., Ducci L., Borkowski J., 2022, GRB Coordinates Network, 32698, 1

Metzger B. D., Margalit B., Sironi L., 2019, Monthly Notices of the Royal Astronomical Society, 485, 4091

Murase K., Kashiyama K., Mészáros P., 2016, Monthly Notices of the Royal Astronomical Society, 461, 1498

Nan R., et al., 2011, International Journal of Modern Physics D, 20, 989

Newburgh L. B., et al., 2014, in Stepp L. M., Gilmozzi R., Hall H. J., eds, Society of Photo-Optical Instrumentation Engineers (SPIE) Conference Series Vol. 9145, Ground-based and Airborne Telescopes V. p. 91454V (arXiv:1406.2267), doi:10.1117/12.2056962

Palm D. M., 2022, The Astronomer's Telegram, 15667, 1

Palmer D. M., BAT Team 2020, GRB Coordinates Network, 27665, 1

Pleunis Z., CHIME/FRB Collaboration 2020, The Astronomer's Telegram, 14080, 1

Qu Y., Zhang B., 2021, arXiv e-prints, p. arXiv:2111.12269

Ridnaia A., et al., 2021, Nat Astron, 5, 372

Scholz P., et al., 2017, ApJ, 846, 80

Tavani M., et al., 2021, Nat Astron, 5, 401

The CHIME/FRB Collaboration 2020, Nature, 587, 54

The CHIME/FRB Collaboration et al., 2018, ApJ, 863, 48

Tyul'bashev S. A., Tyul'bashev V. S., Oreshko V. V., Logvinenko S. V., 2016, Astron. Rep., 60, 220

Wadiasingh Z., Timokhin A., 2019, The Astrophysical Journal, 879, 4

Wadiasingh Z., Beniamini P., Timokhin A., Baring M. G., van der Horst A. J., Harding A. K., Kazanas D., 2020, The Astrophysical Journal, 891, 82

Wang W.-Y., Xu R., Chen X., 2020, ApJ, 899, 109

Wang W.-Y., Yang Y.-P., Niu C.-H., Xu R., Zhang B., 2022a, The Astrophysical Journal, 927, 105

Wang C. W., et al., 2022b, The Astronomer's Telegram, 15682, 1

Yang Y.-P., Zhang B., 2018, The Astrophysical Journal, 868, 31

Yang Y.-P., Zhang B., 2021, The Astrophysical Journal, 919, 89

Yang Y.-P., Zhu J.-P., Zhang B., Wu X.-F., 2020, ApJ, 901, L13

Yang Y.-H., et al., 2021, ApJ, 906, L12

Younes G., et al., 2020, ApJL, 904, L21

Younes G., et al., 2021, Nature Astronomy, 5, 408

Zhang B., 2018, The Physics of Gamma-Ray Bursts. Cambridge University Press, Cambridge, doi:10.1017/9781139226530, https://www.cambridge.org/core/books/physics-of-gammaray-bursts/6B74CFAD4209686DBCAA17D3A7B6E407

Zhang B., 2020, Nature, 587, 45

Zhang B., 2021, ApJ, 907, L17

Zhang B., 2022a, arXiv e-prints, p. arXiv:2212.03972

Zhang B., 2022b, ApJ, 925, 53

Zhang S., et al., 2018, in den Herder J.-W. A., Nikzad S., Nakazawa K., eds, Society of Photo-Optical Instrumentation Engineers (SPIE) Conference Series Vol. 10699, Space Telescopes and Instrumentation 2018: Ultraviolet to Gamma Ray. p. 106991U (arXiv:1910.04434), doi:10.1117/12.2311835

Zhang C. F., et al., 2020, The Astronomer's Telegram, 13699, 1

Table A1. X-ray bursts from SGR J1935+2154 detected in association with radio emission.

#	Telescope	Date	Time (UTC)	T_{90} (s)	Flux[†]
1a	INTEGRAL[1]	2020-4-28	14:34:24.357	0.75	$10.2^{+0.5}_{-0.5}$
1b	HXMT[2]	2020-4-28	14:34:24.011	1.2	$7.14^{+0.41}_{-0.38}$
1c	KW[3]	2020-4-28	14:34:24.447	0.464	$9.7^{+1.1}_{-1.1}$
1d	AGILE[4]	2020-4-28	14:34:24.400	0.5	~ 10
2	GECAM[5]	2022-10-14	19:21:39.100	0.25	—[*]
3	HXMT	2022-10-21	10:01:45	—[*]	—[*]

[†] $(10^{-7} \text{ erg cm}^{-2} \text{ s}^{-1})$.
[*] Data not yet available due to recency of observations at the time of writing.
[1] INTEGRAL detections are provided in the energy range of 20–200 keV (Mereghetti et al. 2020).
[2] HXMT detections are provided in the energy range of 1–250 keV (Li et al. 2021).
[3] Konus-Wind detections are provided in the energy range of 20–500 keV (Ridnaia et al. 2021).
[4] AGILE detections are provided in the energy range of 18–60 keV (Tavani et al. 2021).
[5] GECAM detections are provided in the energy range of 20–100 keV (Wang et al. 2022b).

Zhou D. J., et al., 2022, arXiv e-prints, p. arXiv:2210.03607

Zhu W., et al., 2020, The Astronomer's Telegram, 14084, 1

Zhu W. W., et al., 2022, submitted

Zou J.-H., Zhang B.-B., Zhang G.-Q., Yang Y.-H., Shao L., Wang F.-Y., 2021, ApJL, 923, L30

APPENDIX A: X-RAY DETECTIONS FROM SGR J1935+2154

Table A1 lists the XRBs from SGR J1935+2154 detected in association with radio emission. Table A2 lists the XRBs detected during FAST observing windows of the same source.

APPENDIX B: CHARACTERISTIC SPECTRAL WIDTH OF FRB 200428 REFERENCED TO PEAK FREQUENCY

The two independent detections of FRB 200428 by NICER and CHIME can be used to estimate a characteristic spectral width of FRB 200428 assuming it has a Gaussian spectral shape.

From equation 6,

$$f_{\nu,\text{CHIME}} = f_{\nu,\text{peak}} \exp\left[-\frac{1}{2}\left(\frac{\nu_{\text{CHIME}} - \nu_{\text{peak}}}{\delta\nu}\right)^2\right] \tag{B1}$$

where $f_{\nu,\text{peak}} \approx 1320$ MHz is the peak frequency of FRB 200428 (Extended Data Fig. 1 in Bochenek et al. (2020b)) and $f_{\nu,\text{CHIME}} \approx 600$ MHz is the central observing frequency of CHIME. Solving for $\delta\nu$,

$$\delta\nu = \frac{|\nu_{\text{CHIME}} - \nu_{\text{peak}}|}{2\left[\ln(f_{\nu,\text{peak}}) - \ln(f_{\nu,\text{CHIME}})\right]^{1/2}} \tag{B2}$$

one obtains a characteristic burst spectral width for FRB 200428, $\delta\nu \approx 367$ MHz. Referenced to the peak frequency, $\delta\nu/\nu \approx (367 \text{ MHz})/(1320 \text{ MHz}) = 0.278$.

This paper has been typeset from a TeX/LaTeX file prepared by the author.

Table A2. X-ray bursts from SGR J1935+2154 concurrent with FAST observing windows.

#	Scope	Date	Time (UTC)	T_{90} (s)	Flux[†]	#	Scope	Date	Time (UTC)	T_{90} (s)	Flux[†]
1	Fermi[1]	2020-04-28	00:19:44.192	0.080	$142.75^{+25.00}_{-21.50}$	50	NICER	2020-04-28	00:45:21.543	1.259	$0.25^{+0.02}_{-0.02}$
2	Fermi	2020-04-28	00:23:04.728	0.021	$143.33^{+31.43}_{-29.05}$	51	NICER	2020-04-28	00:45:24.151	1.131	$0.31^{+0.03}_{-0.03}$
3	Fermi	2020-04-28	00:24:30.296	0.122	$2858.93^{+56.48}_{-59.10}$	52	NICER	2020-04-28	00:45:28.849	0.915	$0.21^{+0.03}_{-0.03}$
4	Fermi	2020-04-28	00:25:43.945	0.076	$16.97^{+10.66}_{-9.21}$	53	Fermi	2020-04-28	00:45:31.097	0.030	$213.67^{+32.67}_{-30.33}$
5	Fermi	2020-04-28	00:37:36.153	0.095	$52.63^{+12.00}_{-11.16}$	54	NICER	2020-04-28	00:45:33.729	0.921	$0.13^{+0.03}_{-0.03}$
6	Fermi	2020-04-28	00:39:39.513	0.194	$107.94^{+13.45}_{-10.98}$	55	NICER	2020-04-28	00:45:39.254	0.655	$1.55^{+0.11}_{-0.10}$
7	Fermi	2020-04-28	00:40:33.072	0.190	$188.84^{+15.21}_{-14.89}$	56	NICER	2020-04-28	00:45:42.233	1.484	$0.08^{+0.01}_{-0.01}$
8	NICER[2]	2020-04-28	00:41:21.260	0.194	$0.32^{+0.18}_{-0.12}$	57	NICER	2020-04-28	00:45:43.978	0.259	$0.58^{+0.10}_{-0.07}$
9	NICER	2020-04-28	00:41:23.653	0.088	—*	58	NICER	2020-04-28	00:45:46.842	2.015	$0.50^{+0.04}_{-0.03}$
10	Fermi	2020-04-28	00:41:32.136	0.222	$623.83^{+20.50}_{-20.18}$	59	NICER	2020-04-28	00:45:48.460	0.777	$0.13^{+0.03}_{-0.02}$
11	NICER	2020-04-28	00:41:49.321	0.216	$0.40^{+0.10}_{-0.08}$	60	NICER	2020-04-28	00:45:49.738	0.513	$0.49^{+0.06}_{-0.05}$
12	NICER	2020-04-28	00:41:53.367	0.067	—*	61	NICER	2020-04-28	00:45:51.765	0.289	$0.20^{+0.04}_{-0.03}$
13	NICER	2020-04-28	00:41:56.329	1.453	$0.15^{+0.02}_{-0.02}$	62	NICER	2020-04-28	00:45:56.514	0.962	$0.27^{+0.04}_{-0.03}$
14	NICER	2020-04-28	00:42:00.253	0.225	$0.16^{+0.09}_{-0.06}$	63	NICER	2020-04-28	00:45:57.347	0.088	$3.24^{+0.57}_{-0.48}$
15	NICER	2020-04-28	00:42:01.643	0.538	$2.45^{+0.12}_{-0.11}$	64	NICER	2020-04-28	00:45:58.064	0.544	$0.25^{+0.04}_{-0.03}$
16	NICER	2020-04-28	00:42:14.484	0.462	$0.29^{+0.04}_{-0.04}$	65	Fermi	2020-04-28	00:46:00.009	0.208	$113.17^{+13.80}_{-11.20}$
17	NICER	2020-04-28	00:42:26.739	0.470	$0.10^{+0.03}_{-0.02}$	66	Fermi	2020-04-28	00:46:00.609	0.126	$232.54^{+21.27}_{-18.25}$
18	NICER	2020-04-28	00:42:43.711	0.188	$0.65^{+0.15}_{-0.12}$	67	Fermi	2020-04-28	00:46:06.408	0.019	$228.42^{+44.74}_{-39.47}$
19	NICER	2020-04-28	00:42:48.218	0.249	$0.10^{+0.03}_{-0.02}$	68	NICER	2020-04-28	00:46:08.257	0.602	$0.15^{+0.03}_{-0.02}$
20	NICER	2020-04-28	00:42:52.058	0.985	$2.09^{+0.10}_{-0.09}$	69	NICER	2020-04-28	00:46:12.379	1.277	$0.08^{+0.01}_{-0.01}$
21	NICER	2020-04-28	00:42:54.467	0.274	$6.31^{+0.30}_{-0.28}$	70	NICER	2020-04-28	00:46:14.233	0.840	$0.24^{+0.03}_{-0.03}$
22	NICER	2020-04-28	00:43:01.939	1.521	$0.12^{+0.03}_{-0.02}$	71	NICER	2020-04-28	00:46:18.015	2.852	$1.82^{+0.04}_{-0.04}$
23	NICER	2020-04-28	00:43:10.976	1.923	$0.19^{+0.02}_{-0.02}$	72	Fermi	2020-04-28	00:46:20.176	0.166	$2881.93^{+52.23}_{-55.42}$
24	NICER	2020-04-28	00:43:16.911	0.331	—*	73	Fermi	2020-04-28	00:46:23.504	0.742	$38.49^{+4.95}_{-5.07}$
25	NICER	2020-04-28	00:43:22.492	1.401	$0.36^{+0.04}_{-0.02}$	74	NICER	2020-04-28	00:46:27.415	1.129	$0.25^{+0.02}_{-0.02}$
26	Fermi	2020-04-28	00:43:25.169	0.174	$365.00^{+22.82}_{-20.63}$	75	NICER	2020-04-28	00:46:29.769	1.263	$1.38^{+0.07}_{-0.06}$
27	NICER	2020-04-28	00:43:33.334	0.809	$0.07^{+0.02}_{-0.01}$	76	NICER	2020-04-28	00:46:33.658	3.700	$1.32^{+0.03}_{-0.03}$
28	NICER	2020-04-28	00:43:37.945	2.015	$0.20^{+0.02}_{-0.02}$	77	NICER	2020-04-28	00:46:40.541	1.906	$0.42^{+0.03}_{-0.03}$
29	NICER	2020-04-28	00:43:40.490	0.113	$0.20^{+0.12}_{-0.07}$	78	Fermi	2020-04-28	00:46:43.208	0.128	$265.86^{+20.00}_{-19.38}$
30	NICER	2020-04-28	00:43:42.183	0.146	—*	79	NICER	2020-04-28	00:46:46.829	1.450	$0.20^{+0.02}_{-0.02}$
31	NICER	2020-04-28	00:43:45.240	0.809	$0.21^{+0.04}_{-0.03}$	80	NICER	2020-04-28	00:46:48.887	0.697	$0.29^{+0.05}_{-0.04}$
32	NICER	2020-04-28	00:44:00.180	1.366	$0.17^{+0.02}_{-0.02}$	81	NICER	2020-04-28	00:46:50.557	0.923	$0.45^{+0.04}_{-0.04}$
33	NICER	2020-04-28	00:44:05.104	0.319	$0.20^{+0.05}_{-0.04}$	82	NICER	2020-04-28	00:46:56.705	2.204	$0.87^{+0.04}_{-0.04}$
34	Fermi	2020-04-28	00:44:08.202	0.154	$4698.12^{+81.10}_{-76.69}$	83	NICER	2020-04-28	00:46:59.743	0.904	$1.55^{+0.07}_{-0.07}$
35	Fermi	2020-04-28	00:44:09.302	0.112	$455.98^{+26.07}_{-24.11}$	84	NICER	2020-04-28	00:47:02.017	1.086	$0.48^{+0.05}_{-0.04}$
36	NICER	2020-04-28	00:44:19.570	1.433	$0.19^{+0.02}_{-0.02}$	85	NICER	2020-04-28	00:47:04.505	1.721	$1.05^{+0.05}_{-0.05}$
37	NICER	2020-04-28	00:44:26.236	0.955	$0.28^{+0.03}_{-0.03}$	86	NICER	2020-04-28	00:47:09.756	2.044	$0.17^{+0.02}_{-0.02}$
38	NICER	2020-04-28	00:44:32.458	1.174	$0.23^{+0.03}_{-0.03}$	87	NICER	2020-04-28	00:47:14.611	4.472	$0.52^{+0.02}_{-0.02}$
39	NICER	2020-04-28	00:44:40.056	0.417	$0.16^{+0.04}_{-0.03}$	88	NICER	2020-04-28	00:47:18.948	0.910	$3.16^{+0.15}_{-0.14}$
40	NICER	2020-04-28	00:44:45.286	0.398	$0.34^{+0.05}_{-0.04}$	89	Fermi	2020-04-28	00:47:24.961	0.152	$40.79^{+7.89}_{-6.58}$
41	NICER	2020-04-28	00:44:48.974	1.041	$0.38^{+0.04}_{-0.03}$	90	NICER	2020-04-28	00:47:27.151	0.409	$0.25^{+0.05}_{-0.04}$
42	NICER	2020-04-28	00:44:49.855	0.123	$1.41^{+0.25}_{-0.21}$	91	NICER	2020-04-28	00:47:30.390	0.789	$0.10^{+0.02}_{-0.02}$
43	NICER	2020-04-28	00:44:51.209	0.954	$0.10^{+0.03}_{-0.02}$	92	NICER	2020-04-28	00:47:32.145	0.579	$1.91^{+0.14}_{-0.13}$
44	NICER	2020-04-28	00:44:56.358	0.998	$0.13^{+0.03}_{-0.02}$	93	NICER	2020-04-28	00:47:35.689	0.809	$6.17^{+0.14}_{-0.14}$
45	NICER	2020-04-28	00:44:59.898	0.300	$2.51^{+0.18}_{-0.17}$	94	NICER	2020-04-28	00:47:39.312	0.861	$0.26^{+0.03}_{-0.03}$
46	NICER	2020-04-28	00:45:05.783	0.350	$0.40^{+0.08}_{-0.06}$	95	NICER	2020-04-28	00:47:41.968	0.324	$0.45^{+0.09}_{-0.07}$
47	NICER	2020-04-28	00:45:11.175	0.854	$0.85^{+0.06}_{-0.06}$	96	NICER	2020-04-28	00:47:43.459	0.157	—*
48	NICER	2020-04-28	00:45:12.122	0.365	$0.38^{+0.07}_{-0.06}$	97	NICER	2020-04-28	00:47:44.331	1.941	$0.32^{+0.02}_{-0.02}$
49	NICER	2020-04-28	00:45:20.845	0.145	—*	98	NICER	2020-04-28	00:47:47.056	0.826	$0.15^{+0.03}_{-0.03}$

Table A2. Continued.

#	Scope	Date	Time (UTC)	T_{90} (s)	Flux[†]
99	NICER	2020-04-28	00:47:52.328	0.719	$3.31^{+0.16}_{-0.15}$
100	NICER	2020-04-28	00:47:56.536	0.136	$0.32^{+0.18}_{-0.07}$
101	Fermi	2020-04-28	00:47:57.528	0.084	$141.31^{+14.29}_{-13.21}$
102	NICER	2020-04-28	00:48:00.243	1.446	$2.34^{+0.05}_{-0.05}$
103	NICER	2020-04-28	00:48:08.251	0.453	$1.51^{+0.15}_{-0.10}$
104	NICER	2020-04-28	00:48:23.754	3.508	$0.17^{+0.01}_{-0.01}$
105	NICER	2020-04-28	00:48:27.020	1.129	$1.55^{+0.07}_{-0.07}$
106	NICER	2020-04-28	00:48:33.367	0.938	$2.34^{+0.11}_{-0.11}$
107	Fermi	2020-04-28	00:48:44.824	0.382	$62.36^{+10.73}_{-9.32}$
108	Fermi	2020-04-28	00:48:49.272	0.112	$730.45^{+41.34}_{-34.91}$
109	NICER	2020-04-28	00:48:56.199	3.788	$1.17^{+0.03}_{-0.03}$
110	Fermi	2020-04-28	00:49:00.273	0.120	$49.00^{+10.00}_{-10.25}$
111	Fermi	2020-04-28	00:49:01.121	0.151	$80.60^{+11.13}_{-10.13}$
112	Fermi	2020-04-28	00:49:01.936	0.181	$58.23^{+13.09}_{-12.15}$
113	Fermi	2020-04-28	00:49:06.472	0.022	$75.91^{+21.36}_{-20.00}$
114	Fermi	2020-04-28	00:49:16.592	0.234	$176.24^{+14.06}_{-11.79}$
115	Fermi	2020-04-28	00:49:22.392	0.078	$80.51^{+10.64}_{-9.87}$
116	Fermi	2020-04-28	00:49:27.280	0.082	$43.41^{+11.22}_{-9.39}$
117	NICER	2020-04-28	00:49:32.702	0.821	$0.45^{+0.04}_{-0.03}$
118	NICER	2020-04-28	00:49:34.115	0.853	$0.79^{+0.06}_{-0.05}$
119	NICER	2020-04-28	00:49:35.948	0.799	$3.39^{+0.16}_{-0.15}$
120	NICER	2020-04-28	00:49:36.957	1.281	$0.17^{+0.02}_{-0.02}$
121	NICER	2020-04-28	00:49:40.293	2.106	$0.32^{+0.02}_{-0.02}$
122	NICER	2020-04-28	00:49:42.741	1.408	$0.52^{+0.04}_{-0.04}$
123	Fermi	2020-04-28	00:49:46.142	0.036	$44.17^{+13.61}_{-12.22}$
124	Fermi	2020-04-28	00:49:46.680	0.150	$144.13^{+18.53}_{-20.93}$
125	NICER	2020-04-28	00:49:50.079	0.484	$0.27^{+0.05}_{-0.03}$
126	NICER	2020-04-28	00:49:52.271	2.119	$0.83^{+0.04}_{-0.04}$
127	NICER	2020-04-28	00:49:55.078	1.197	$0.44^{+0.03}_{-0.03}$
128	Fermi	2020-04-28	00:50:01.012	0.047	$140.21^{+20.64}_{-18.51}$
129	Fermi	2020-04-28	00:50:01.358	0.095	$279.05^{+20.42}_{-25.16}$
130	NICER	2020-04-28	00:50:03.786	0.803	$1.48^{+0.11}_{-0.10}$
131	NICER	2020-04-28	00:50:05.664	0.440	$0.72^{+0.07}_{-0.05}$
132	NICER	2020-04-28	00:50:09.487	0.424	$0.43^{+0.07}_{-0.06}$
133	NICER	2020-04-28	00:50:11.182	0.624	$0.17^{+0.03}_{-0.02}$
134	NICER	2020-04-28	00:50:14.097	1.952	$0.29^{+0.02}_{-0.02}$
135	NICER	2020-04-28	00:50:17.529	1.172	$0.59^{+0.04}_{-0.04}$
136	Fermi	2020-04-28	00:50:21.969	0.019	$70.53^{+30.53}_{-25.79}$
137	NICER	2020-04-28	00:50:30.726	0.237	$0.16^{+0.09}_{-0.03}$
138	NICER	2020-04-28	00:50:34.936	0.674	$1.95^{+0.09}_{-0.09}$
139	HXMT[3]	2020-05-06	22:48:21.550	0.035	$7.60^{+1.40}_{-1.50}$
140	HXMT	2020-05-12	21:47:43.340	0.015	$10.00^{+2.20}_{-1.90}$

[†] (10^{-8} erg cm^{-2} s^{-1}).

[*] Flux data not reported.

[1] Fermi detections are provided in the energy range of 8 keV–1 MeV (Yang et al. 2021).

[2] NICER detections are provided in the energy range of 0.5–10 keV (Younes et al. 2020).

[3] HXMT detections are provided in the energy range of 1–250 keV (Cai et al. 2022b).